
 Research
 Additive Manufacturing—Article

Design and *In Situ* Additive Manufacturing of Multifunctional Structures

 Yan Zhang^a, Guangyu Zhang^a, Jing Qiao^{b,*}, Longqiu Li^{a,*}
^a State Key Laboratory of Robotics and System, Harbin Institute of Technology, Harbin 150001, China

^b School of Materials Science and Engineering, Harbin Institute of Technology, Harbin 150001, China


ARTICLE INFO

Article history:

Received 22 November 2021

Revised 16 September 2022

Accepted 9 November 2022

Available online 06 April 2023

Keywords:

Additive manufacturing

Multifunctional structure

Optimal design

Satellite

Polyetheretherketone

ABSTRACT

Multifunctional structures (MFSs) integrate diverse functions to achieve superior properties. However, conventional design and manufacturing methods—which generally lack quality control and largely depend on complex equipment with multiple stations to achieve the integration of distinct materials and devices—are unable to satisfy the requirements of MFS applications in emerging industries such as aerospace engineering. Motivated by the concept of design for manufacturing, we adopt a layer regulation method with an established optimization model to design typical MFSs with load-bearing, electric, heat-conduction, and radiation-shielding functions. A high-temperature *in situ* additive manufacturing (AM) technology is developed to print various metallic wires or carbon fiber-reinforced high-melting-point polyetheretherketone (PEEK) composites. It is found that the MFS, despite its low mass, exceeds the stiffness of the PEEK substrate by 21.5%. The embedded electrics remain functional after the elastic deformation stage. Compared with those of the PEEK substrate, the equivalent thermal conductivity of the MFS beneath the central heat source area is enhanced by 568.0%, and the radiation shielding is improved by 27.9%. Moreover, a satellite prototype with diverse MFSs is rapidly constructed as an illustration. This work provides a systematic approach for high-performance design and advanced manufacturing, which exhibits considerable prospects for both the function expansion and performance enhancement of industrial equipment.

© 2023 THE AUTHORS. Published by Elsevier LTD on behalf of Chinese Academy of Engineering and Higher Education Press Limited Company. This is an open access article under the CC BY-NC-ND license (<http://creativecommons.org/licenses/by-nc-nd/4.0/>).

1. Introduction

The use of multifunctional structures (MFSs)—which integrate a wide array of functional capabilities such as load-bearing [1], electric [2], and thermal-conductivity [3] capacities in one structure—can prevent the need for most bolted mechanical interfaces and reduce the volume of the total system. Thus, MFSs offer excellent prospects for industries such as aerospace, aviation, and intelligent equipment [4–7]. For example, satellite structures, which perform multiple functions in addition to supporting payloads and subsystems at different stages of spacecraft life, can be classified as MFSs to some extent [8,9]. Such structures should provide heat conduction to allow heat sources to dissipate heat, ensure connections for electronic devices, and help protect devices from cosmic environmental damage (e.g., radiation shielding) [10]. In particular, nano-satellites are subject to size restrictions, so developing MFSs that can effectively solve the contradiction between a tiny volume

and rich contents is of great interest for the aerospace industry [11,12].

There are two important steps in developing an excellent MFS: design and manufacturing [13]. Compared with a single structural part, however, an MFS involves the integration of multiple components, as it requires containers for the subsystem hardware, mechanical interfaces, frames, bulky wire harnesses, and so forth [8]. Therefore, it is complicated to design and manufacture an MFS in response to various requirements. Diverse-function-integration design and subsequent convenient manufacturing play a vital role in driving the evolution of MFS technology and promoting its widespread applications [14,15].

The design of an MFS must consider the reasonable layout of different functions in a single structure within a limited space. Research has been carried out to determine the design of various functional components in order to maximize space utilization [9,11,16,17]. For example, Ikeya et al. [9] employed MFSs in nano-satellites and achieved a highly compact layout by stitching wire fibers and gluing solar cells and antennas to the membrane surface. The structure offered innovative insights into space systems by

* Corresponding authors.

E-mail addresses: jingqiao@hit.edu.cn (J. Qiao), longqiuli@hit.edu.cn (L. Li).

utilizing deployable membranes to achieve array antennas and solar array integration. Galos et al. [16] directly embedded LiPo batteries into sandwich composites to save space. The researchers found that MFS design can simultaneously achieve the two functions of load bearing and energy storage. However, these representative works lacked mass control despite achieving a compact arrangement of volume, and even added a significant quantity to the total mass, because the density of embedded functional devices is often higher than that of the substrates, which is a disadvantage in aerospace applications. In addition, more applicable and richer categories of functions should be designed and contained to make MFSs suitable for complex space environments. The concept of design for additive manufacturing (DfAM) can be referenced to include more function types by means of layer regulation conforming to manufacturing features [18,19]. On this basis, establishing an optimization model that balances multifunctional quantitative description with structural volume and mass is necessary. Unfortunately, existing optimization models—which tend to focus on structural parts and their mechanical properties—cannot be used to strike a balance between different functional components in terms of location distribution and performance compromise within a limited volume.

The integration of independent functional components within a single structure increases not only the design difficulty but also the fabrication complexity [20,21]. Additive manufacturing (AM), also known as three-dimensional (3D) printing, is an efficient and flexible method for manufacturing complex MFSs [22–27]. Based on the rapid prototyping of complex shapes with layer-by-layer building, composite printing technologies are constantly developing with growing performance requirements. For satellite structures, Espalin et al. [28] and MacDonald et al. [29] employed a thermal-assisted technology to submerge copper wires into polymer substrates in order to print metallic circuits. They found that metallic wires showed better robustness than conductive inks. Nevertheless, extra heating effects can easily change the polymer morphology as well as the mechanical properties. Moreover, traditional fabrication methods require multiple processes and stations but can only print resin or metals at one time [30]. Thus, developing an *in situ* fabrication method to produce one structure with multiple functions is attractive, because it can greatly reduce the processing errors caused by conversion among different stations and improve fabrication efficiency [31]. However, simultaneously printing multiple materials such as polymers and metals for functional devices remains challenging, as the exclusive morphologies and properties of distinct materials correspond to different processing conditions [32]. In particular, high-temperature printing technology is desirable for fabricating MFSs for satellite structures in order to soften the materials, which include metal and high melting-point polymers such as polyetheretherketone (PEEK). However, PEEK exhibits inferior printability, even though it has excellent comprehensive properties that meet stringent environmental testing standards [33–36].

As can be seen from this literature review, developing MFSs that can achieve powerful function integration and significant performance improvement is of particular interest to the aerospace industry. Unfortunately, it is challenging to adopt a systematic approach to design and manufacture such MFSs to meet diverse deployment scenarios. Existing MFS designs generally ignore mass control and even inadvertently increase the overall mass by embedding functional devices with a higher density into the substrates. Moreover, conventional MFS manufacturing methods usually require additional equipment and multiple stations to assist in collaboration, as the applied single printers can only fabricate either resin or metal at one time. In particular, to the best of our knowledge, no study has considered a high-temperature *in situ* printing technology that simultaneously combines resin and metal for fabricating MFSs.

The objective of this work is to address the abovementioned issues related to MFSs. First, a typical panel structure is designed based on layer regulation and multifunctional optimization to incorporate the diverse functions of load bearing, electronics, heat conduction, and radiation protection. The MFSs are subsequently manufactured *in situ* by the developed high-temperature coaxial extrusion equipment, according to a detailed process and path planning. Then, the performances of the fabricated MFSs are systematically investigated through a combination of experiments and simulations. Furthermore, following the proposed feasible technical route, a satellite prototype is constructed as an illustration by assembling different MFSs embedded with various modules (e.g., sensing and communication).

2. Concept and design

The panel structure is a typical basic unit of advanced equipment. Here, satellites are taken as an illustration, and an MFS panel for satellite applications is depicted in Fig. 1(a). In addition to having its own independent functional systems, the MFS panel can also interact with other MFSs through the interface to form a complete satellite. The design and rapid fabrication of MFSs offer the possibility of reconstructing large satellites in orbit and providing space maintenance for damaged spacecraft.

The design of the MFS is based on the layer-by-layer nature of AM; it includes a layout with different layer types and the determination of specific design parameters. The layout of the MFS is shown in Fig. 1(b). To limit the weight as the functions increase, a sandwich structure is adopted for the MFS panel. The panel (overall size: 120.0 mm × 120.0 mm × 9.5 mm) integrates the functions of load bearing, electrics, heat conduction, and radiation protection, according to an aerospace application. The lowest layers (corresponding to the outermost layers after assembly) are PEEK composites with woven aluminum wires, which are intended to improve the mechanical properties, radiation resistance, and heat-dissipation coefficient of the PEEK substrate. Adjacent to the outermost layers, the sandwich core is reinforced with carbon fiber (CF) for strength enhancement and weight reduction. The center space in the core is filled with four aluminum blocks to transmit heat directly from the upper layers to the lower layers. The core is covered by a CF-reinforced polymer (CFRP) coating layer. After sealing the core, the copper wires and chips are laid out. Copper gaskets are placed at the ends of circuit wires to expand the conductive contact area. A silicone sheet with thermal conduction and electrical insulation is placed between the aluminum blocks and controller. Finally, the upper layers of the circuit are encapsulated with pure PEEK resin.

The MFS panel is divided into five types of layers according to the components, as shown in Fig. 1(b). With the given overall layout, the design parameters for the layer thickness distribution must be determined to ensure that the MFS exhibits excellent performance with a combination of load bearing, electronics, heat conduction, and radiation shielding. Thus, the optimization objective can be expressed as follows:

$$\max_{\mathbf{X}, n \in \mathbb{N}^*} F(\mathbf{X}) = [M(\mathbf{X}), L(\mathbf{X}), H(\mathbf{X}), R(\mathbf{X})] \quad (1)$$

where the objective function $F(\mathbf{X})$ represents the performance related to mechanical properties $M(\mathbf{X})$, electricity $L(\mathbf{X})$, heat conduction $H(\mathbf{X})$, and radiation shielding $R(\mathbf{X})$; $\mathbf{X} = [x_1, x_2, x_3, x_4, x_5]$ is the design variable; n is the subscript of the element in \mathbf{X} ; and \mathbb{N}^* represents the positive integer.

The different function indexes $M(\mathbf{X})$, $L(\mathbf{X})$, $H(\mathbf{X})$, and $R(\mathbf{X})$ represent the relative performance improvement of the corresponding function compared with the pure PEEK structure, and representative indicators are selected. Combined with constraints, the

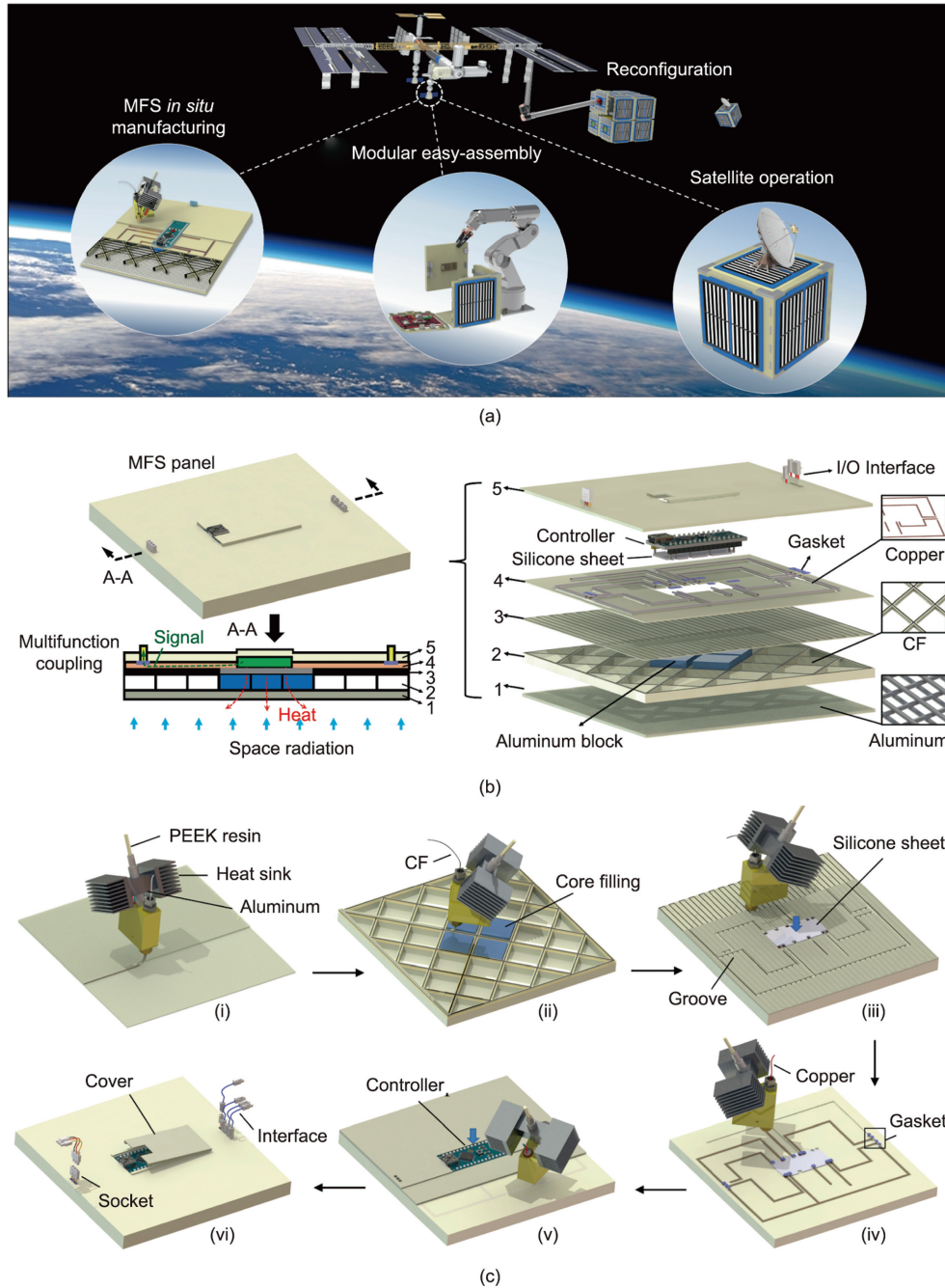


Fig. 1. Description and concept of the MFS. (a) Concept design of the MFS in aerospace, where a single MFS design, manufacturing, and diverse panel assembly constitute the satellite; (b) functional configuration and structural explosion diagram of the MFS, where numbers 1–5 indicate the type order of functional layers (descriptions are listed in Table 2); (c) description of the MFS process design. I/O: input/output; CF: carbon fiber; A–A represents central-section.

optimization process is presented by Eqs. (S1)–(S24) in Appendix A. By applying a genetic algorithm and convergence analysis, the thickness of each layer type can be determined to be 1.5, 4.0, 0.5, 0.5, and 3.0 mm, as shown in Table 1.

As illustrated in Fig. 1(c), the process design provides a guide for subsequent fabrication. The composite layers with aluminum wire mesh at the bottom are printed first, as shown in (i) in Fig. 1(c). The printing directions of the adjacent layers are perpendicular to each other to form a weaving effect. Then the continuous filler of aluminum wire is replaced with CF (1K, T300, Toray Corp., Japan). The honeycomb core is printed, and four aluminum blocks are placed in the center space of the core, as shown in (ii) in Fig. 1(c). After the core is completed, a CFRP coating layer is fabricated to

cover the core with hanging printing due to the tension of the continuous fiber and the viscosity of the PEEK. One pure PEEK layer is subsequently printed on the CFRP coating, and a designed groove is reserved for the silicone sheet and circuit, as shown in (iii) in Fig. 1(c). A copper wire reinforced filament is printed into the groove, and copper wire gaskets are placed at the ends of the copper wire, as shown in (iv) in Fig. 1(c). Next, the pure resin is extruded as a coating, and a control system is inserted. An Arduino Nano—a board containing microprocessors and controllers—is used here as a representative controller system. The board pins are placed in contact with the copper gaskets to transmit signals to the outside, as shown in (v) in Fig. 1(c). Finally, the interfaces and sockets are plugged in to establish a connection between the internal

Table 1
Design description and parameters of printed layers in the MFS.

Layer type order	Components	Thickness (mm)	Function	Path planning
1	Aluminum, PEEK	1.5	Improvement in stiffness, radiation resistance, and heat dissipation	Continuous zigzag path
2	CF, PEEK	4.0	Weight reduction and strength enhancement	Continuous crossing path
3	CF, PEEK	0.5	Core cover	Continuous zigzag path
4	Copper, PEEK	0.5	Electric signal transmission	DQN reinforcement learning and zigzag path
5	PEEK	3.0	Encapsulation and insulation	Continuous zigzag path

DQN: deep Q network.

embedded circuits and the external connectors. A cover printed according to the controller shape is put on. This completes the *in situ* fabrication of the MFS, as shown in (vi) in Fig. 1(c).

3. Research method

3.1. Mechanical and electrical testing

Panel structures are vulnerable to bending loads. A quasi-static loading with a low-speed head (i.e., $5 \text{ mm}\cdot\text{min}^{-1}$) was applied to the MFS by a universal testing machine (AG-X plus, Shimadzu, Japan), as shown in Fig. S1 in Appendix A. In the experiments, the embedded controller was programmed to send signals to the externally connected device through the printed circuit to verify the operation of the integrated electrical function. In addition, a megohmmeter (1000 V, 1000 M Ω) was used to measure the insulation and leakage between the MFS substrate and the internal circuit, as illustrated in Fig. S2 in Appendix A.

Dynamics tests for modal analysis were applied via impact hammer tests, as shown in Fig. S1(b) in Appendix A. There are 64 equidistant sampling points on the MFS panel, and each point was struck with an impulse impact hammer (9724A5000, Kistler, Switzerland) until at least five effective knocks were made. The accelerometer attached to the suspended panel imported the vibration data into the LMS Test Lab platform for analysis.

3.2. Thermal analysis

The heat transfer process of the MFS was investigated by employing the finite-element method (FEM). The parts were meshed using DC3D8 elements. The thermal properties were measured using a laser flash analyzer (LFA467, NETZSCH, Germany) and a thermal dilatometer (DIL 402 Expedis, NETZSCH). The properties obtained at room temperature (25 °C) are summarized in Table 2. In addition to room temperature, the thermal properties of the printed materials were measured at temperatures from –55 to 125 °C at intervals of 30 °C (Fig. S3 in Appendix A), with the relative humidity controlled below 45%. Here, the properties of the extruded filament are simplified as transverse isotropy.

Table 2
Mechanical and thermal properties of the materials in the MFS measured at 25 °C.

Extruded materials	Poisson's ratio	Young's modulus (GPa)	Thermal conductivity ($\text{W}\cdot\text{m}^{-1}\cdot\text{K}^{-1}$)	Specific heat capacity ($\text{J}\cdot\text{g}^{-1}\cdot\text{K}^{-1}$)
PEEK	0.37	3.1100	0.25	1.52
Aluminum composite	0.31 (longitudinal)	4.6500 (longitudinal)	0.29	1.40
	0.35 (transverse)	3.4100 (transverse)		
CF composite	0.28 (longitudinal)	5.2600 (longitudinal)	0.26	1.41
	0.34 (transverse)	3.0200 (transverse)		
Copper composite	0.30 (longitudinal)	4.8900 (longitudinal)	0.32	1.36
	0.34 (transverse)	3.1500 (transverse)		
Silicon sheet	0.44	0.0035	8.00	1.20
Aluminum block	0.33	68.0000	220.00	0.88

3.3. Radiation-shielding calculation

The Stopping and Range of Ions in Matter (SRIM) program based on the Monte Carlo method was applied to simulate the radiation shielding of the MFS implanted with protons [37]. After verifying the applied calculation program (Fig. S4 in Appendix A), 5000 protons with 35 MeV ($1 \text{ eV} = 1.602 \times 10^{-19}$) were implanted into the central area of the MFS and PEEK panels at an incident angle of 0 from the outside, respectively. The tracks of the proton implantation, along with the panel thickness and the relevant damage, were calculated and analyzed.

4. Manufacturing process

The equipment for MFS manufacturing is shown in Fig. 2(a). The use of an insulation cavity to control the printing environment temperature is a key factor to ensure the formation quality. As shown in the schematic in Fig. 2(b), the printing system inside the cavity was developed to print the polymer and other reinforcements—including CF or metal wires—simultaneously. However, the high temperature during printing will impair the protective sizing agent of the fiber coating, and the CFs are easily scrapped and cut off when they slide over the corners and sharp inner walls of the printing head. Moreover, the larger cross-sectional area of the metal wire takes up more space at the nozzle than the soft CF, which leads to an increase in the chamber pressure that drives the molten resin to flow back along the gap between the filament and the feeding tubes. These issues are demonstrated and addressed in Eqs. (S25)–(S35) in Appendix A. The printing head was machined based on the coaxial extrusion principle. The PEEK resin and continuous fillers enter through two inlets and are then extruded from one nozzle, according to the coaxial design. The diameters of the filler inlet (in the form of a concentric tube) and nozzle can be varied within 0.5–0.8 and 1.0–1.5 mm, respectively. Proportional–integral–derivative (PID) control was adopted for the temperature control of the printing head, with a heating temperature of up to 500 °C.

As the designed MFS involved a variety of composites and the developed printing equipment applies different printing processes,

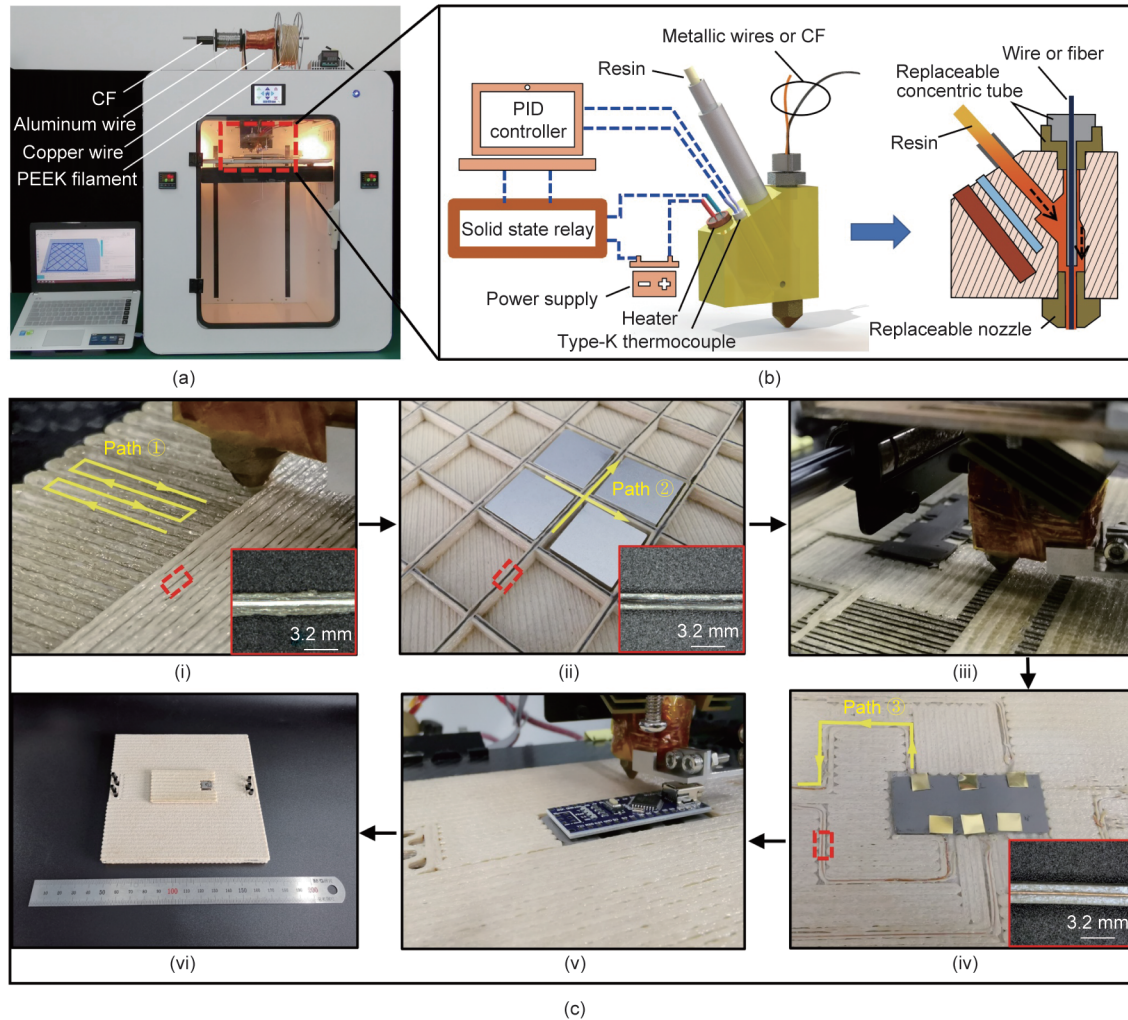


Fig. 2. MFS manufacturing equipment and process. (a) Manufacturing equipment; (b) schematic of the printing system; (c) *in situ* manufacturing process of the MFS corresponding to the process design shown in Fig. 1(c), where ① is a zigzag path, ② is a crossing path, and ③ is a path generated by DQN. PID: proportional–integral–derivative.

it was difficult to use existing commercial or open-source slicing software to directly generate suitable printing paths. Therefore, we applied customized printing paths to adapt to the design and assist manufacturing, as demonstrated in Fig. S5 in Appendix A.

Following the guidance of the path planning and process design, the MFS fabrication is shown in Fig. 2(c). The fabrication process parameters are shown in Table 3. It was found that the porosity of the composites was reduced and was lower than that of the pure PEEK samples. This finding can be attributed to the fact that the filling of the reinforcements results in an increase in the pressure of material extrusion, which makes the fabricated structure denser. The final average mass of the fabricated MFSs was 160.9 g, which was slightly less than that of the pure PEEK panels (i.e., 162.5 g).

The continuous fillers—including aluminum, copper wire, and CF—were successfully extruded in the composite filaments. In

comparison with traditional subtractive manufacturing and the emerging multi-process manufacturing for MFSs in Refs. [29,30], only one-step AM was implemented here. A comparison of the manufacturing processes used herein with those used in Ref. [30] is shown in Fig. 3. It should be noted that coaxial extrusion technology was initially employed to fabricate the soft fiber-reinforced polymer based on conventional thermoplastics, such as polylactic acid (PLA) [38–40] and acrylonitrile-butadiene-styrene (ABS) [41,42], but the metallic wires often could not be embedded because it was difficult to bend the stiff wires and extrude them with the liquid resin. However, the processing temperature (420 °C) for PEEK printing is approximately double (or even more) that of conventional thermoplastics [43–45], which consequently facilitated the softening of the metallic wires. Moreover, the molten PEEK resin has high viscosity, making it easy to stick and fix the

Table 3
Fabrication process parameters and obtained material porosities of different extruded filaments.

Extruded materials	Printing speed (mm·min ⁻¹)	Nozzle temperature (°C)	Average layer thickness (mm)	Porosity
PEEK	300	410	0.5	8.6%
Aluminum composite	250	420	0.5	2.7%
Copper composite	200	420	0.5	1.5%
CF composite	300	410	0.5	5.2%

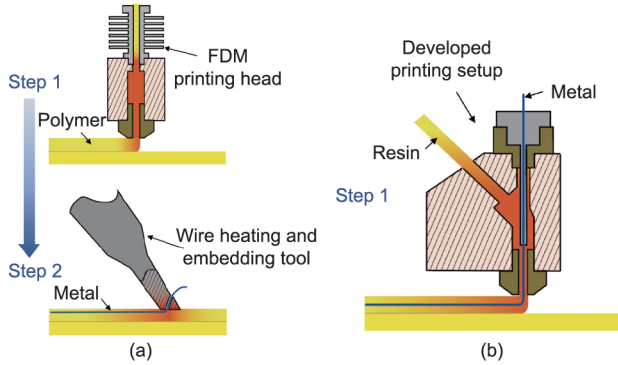


Fig. 3. Fabrication process of polymer composites with embedded metal wire. (a) Two-step fabrication using different equipment in Ref. [30]; (b) one-step high-temperature printing using a developed setup in this work. FDM: fused deposition modeling.

resin to the wire. The composite filament composed of a metal core and PEEK coating is an ideal material for the MFS. A comparison of the fabrication processes is provided in Table 4 [30,46,47]. The developed manufacturing equipment can not only simplify the fabrication process but also produce metal wires with large diameters and diverse types.

5. Results and discussion

5.1. Performance evaluation

5.1.1. Mechanical and electrical response

5.1.1.1. Quasi-static loading. As described in Section 4, the fabricated MFS panel was subjected to quasi-static loading with a low-speed head. The representative deformation and damage behaviors of the MFS panel at different stages are shown in Fig. 4(a). The embedded Arduino was powered and initially operated with the red light on. The input/output (I/O) interfaces of the panel are connected to an external green light-emitting diode (LED), and the controller in the panel sends signals to cause this LED to glow. The excellent insulation between the MFS substrate and the circuits was verified using a megohmmeter; the device's pointer was at the infinity position, indicating no current leakage.

As shown in (i) and (ii) in Fig. 4(a), the light status demonstrates the effectiveness of the fabricated electronics in the MFS. With the loading progress at approximately 2 min, the MFS bends and distinct delamination could be observed, as shown in (iii) in Fig. 4(a). The external signal LED was off, while the light of the embedded Arduino was on. The strength of the layer-stacking direction is much lower than that of the other two in-plane directions, as shown in Fig. S6 in Appendix A. This is the main reason for delamination during structural deformation and failure. MFS delamination leads to inadequate contact between the wires and gaskets, and a large deformation can even lead to circuit fracture;

both of these issues may result in signal interruption of the external LED. However, the Arduino continued to function because of the soft silicone cushion and the hard aluminum block support under the board. At 2 min and 40 s, the MFS experienced substantial bending and delamination, and the Arduino stopped functioning, as shown in (iv) in Fig. 4(a).

The force–displacement curve during loading is shown in Fig. 4(b); the figure also includes the PEEK curve for comparison. The average stiffness (i.e., the slope of the line between the maximum point and origin) of the MFS is approximately 21.5% higher than that of the PEEK structure. This difference is attributed to the filler reinforcement of metal wires and CFs. However, it is easy for the heterogeneous layers and various embedding components to cause damage initiation and delamination; thus, the maximum load of the MFS is lower than that of PEEK. After reaching the maximum, the downward trend of the MFS curve is slower than that of PEEK. The parameter specific energy absorption (SEA) can be used to characterize the process, where SEA is defined as the ratio of absorbed energy to mass during the loading process. It is expressed as follows:

$$SEA = \frac{E_A}{m} \tag{2}$$

$$E_A = \int_0^l P(\delta)d\delta \tag{3}$$

where m is the mass of the structure; $P(\delta)$ is the load corresponding to the displacement δ ; l is the final displacement; and E_A is the energy absorbed.

Fig. 4(c) compares the maximum load and SEA of MFS and PEEK. Despite having a lower maximum load than PEEK, the MFS has better energy-absorption properties. Considering the aeronautical zero-gravity environment, the demand for load-bearing capacity is reduced. The higher energy absorption of MFS is ascribed to the combination of diverse energy-dissipation mechanisms, such as interfacial slip between filler and resin, fracture of the reinforced composites, and layer delamination. The interaction of different mechanisms is also reflected in the fluctuation of the MFS curve in Fig. 4(b) during the damage process. Moreover, the elastic deformation of the MFS occurs within a displacement of 4.75 mm (at 57 s). Considering the LED status at 60 s in (ii) in Fig. 4(a), the electronics can continue to work after the end of the elastic deformation stage.

5.1.1.2. Dynamics analysis. According to the acceleration data obtained through impact hammer tests, the vibration amplitudes of sampling points on the panel are accumulated. The structural response curves at different frequencies are obtained, as shown in Fig. 4(d). Compared with the curve of the PEEK panel, the MFS curve exhibits more fluctuations. As suggested by the damage behaviors of the MFS in the quasi-static tests, the adhesion of layers may be inferred to be weak, and various functional components in each layer produce their own vibration response instead of

Table 4
Comparison of fabrication processes of a polymer substrate with embedded wire.

Required basic steps	Equipment	Embedded wire diameter (mm)	Substrate and printing temperature	Ref.
One	High-temperature coaxial extrusion equipment	0.400 (copper) 0.500 (aluminum)	PEEK (~420 °C)	This work
Two	Stratasys uPrint SE plus, wire heating and embedding tool	0.290 (copper)	ABS (< 230 °C)	Kim et al. [46]
Two	Stratasys Fortus 400mc, ultrasonic embedding gantry	0.127 (copper)	Polycarbonate (< 350 °C)	MacDonald et al. [30]
Two	FFF printer, wire embedding tool	0.320 (copper)	ABS (< 350 °C)	Kim et al. [47]

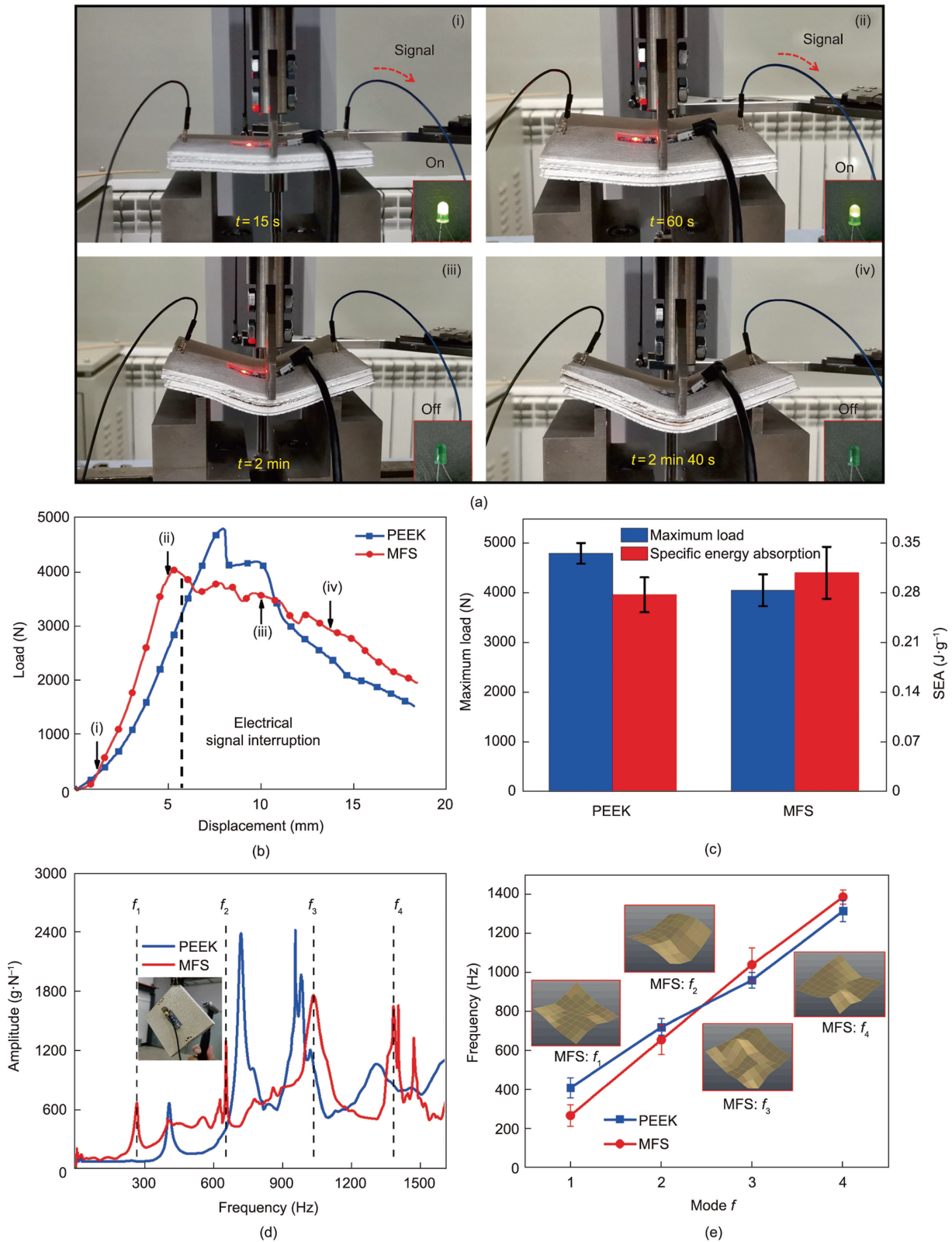


Fig. 4. Mechanical property analysis and embedded circuit verification. (a) Deformation behaviors of MFS under a quasi-static load and working state indication of embedded electronics; (b) force–displacement curves during the loading process; (c) maximum load and energy-absorption comparisons; (d) dynamic responses of amplitude–frequency curves; (e) first four natural frequencies and modes (f_1 – f_4).

showing a harmonious overall structural response similar to that of the pure PEEK structure. The PEEK curve clearly fluctuates and has prominent peaks, especially in the second and third orders.

The first four resonance frequencies of the panels were obtained according to a modal shape analysis at different peaks, as shown in Fig. 4(e). The device embedment and material distribution change

the vibration characteristics. The first two frequencies of the MFS (i.e., 267 and 655 Hz) are lower than those of pure PEEK (409 and 720 Hz, respectively), whereas the third and fourth natural frequencies of the MFS (1037 and 1384 Hz) slightly exceed those of pure PEEK (958 and 1306 Hz, respectively). For aerospace applications, the dynamics of structures must satisfy the vibration requirements. According to consulted reference standards [48,49], the MFS frequencies satisfy all requirements.

5.1.2. Heat conduction

The equivalent thermal conductivity of the MFS beneath the controller was measured using a laser flash analyzer. For comparison, the thermal conductivity of the printed PEEK panel was measured to be $0.25 \text{ W}\cdot\text{m}^{-1}\cdot\text{K}^{-1}$, whereas the equivalent thermal conductivity of the MFS along the thickness direction is $1.67 \text{ W}\cdot\text{m}^{-1}\cdot\text{K}^{-1}$. Despite the impairing and weakening of the interfaces among different components in the MFS, the equivalent thermal conductivity of the MFS was found to be increased by 568% compared with that of the PEEK structure. This improvement is essential for heat to transfer from the inside to the outside along the thickness direction.

To clearly analyze the heat conduction process, a finite-element model was established, as shown in Fig. 5(a). The radiative heat dissipation of the structures was included, and the surface radiation emissivity was set to 0.95 [50]. For observation convenience, the half part cut off by the central section, A–A, was illuminated. Heat is transferred from the upper layers to the lower layers and then radiates to the environment. In the initial state, the heat source in the center of the upper layers was set to $200 \text{ }^\circ\text{C}$, which

is within the PEEK substrate operating temperature; the ambient temperature under the lower layers was set to $-50 \text{ }^\circ\text{C}$. Fig. 5(b) displays the structural temperature fields at representative times (0.5, 2.0, 8.0, and 32.0 s). The heat transfer rate along the transverse direction in the MFS is lower than that along the thickness direction. Thus, the MFS design benefits the heat conduction and dissipation of the embedded controller in the central area.

The temperature values of element points from point O to point D were output, as shown in Figs. 5(c) and (d). The MFS curve tends to flatten with time, and the temperature values at 32 s are relatively consistent. In contrast, the temperature gradient in the PEEK panel remains high. As heat radiates into space, the curves will eventually fall to the $-50 \text{ }^\circ\text{C}$ line. Due to the improved thermal conductivity, heat is quickly and evenly distributed in the MFS, which may prevent the deterioration of material properties caused by heat concentration.

5.1.3. Radiation shielding

The MFS panel was designed to provide enhanced protection capability to prevent the exposure of internal electronics to space irradiation. A large number of protons exist in near-earth orbits [51]. Calculated using the SRIM program, the results of the proton track along the thickness direction are shown in Fig. 6; the red dots in Figs. 6(a) and (d) represent the positions where the protons finally stop. The average implantation depth is defined as the average thickness of all ions passing through the panel, and the corresponding values for the MFS and PEEK panels are 6.74 and 9.35 mm, respectively. Although the PEEK material is suitable for aerospace applications and can absorb radiation energy through

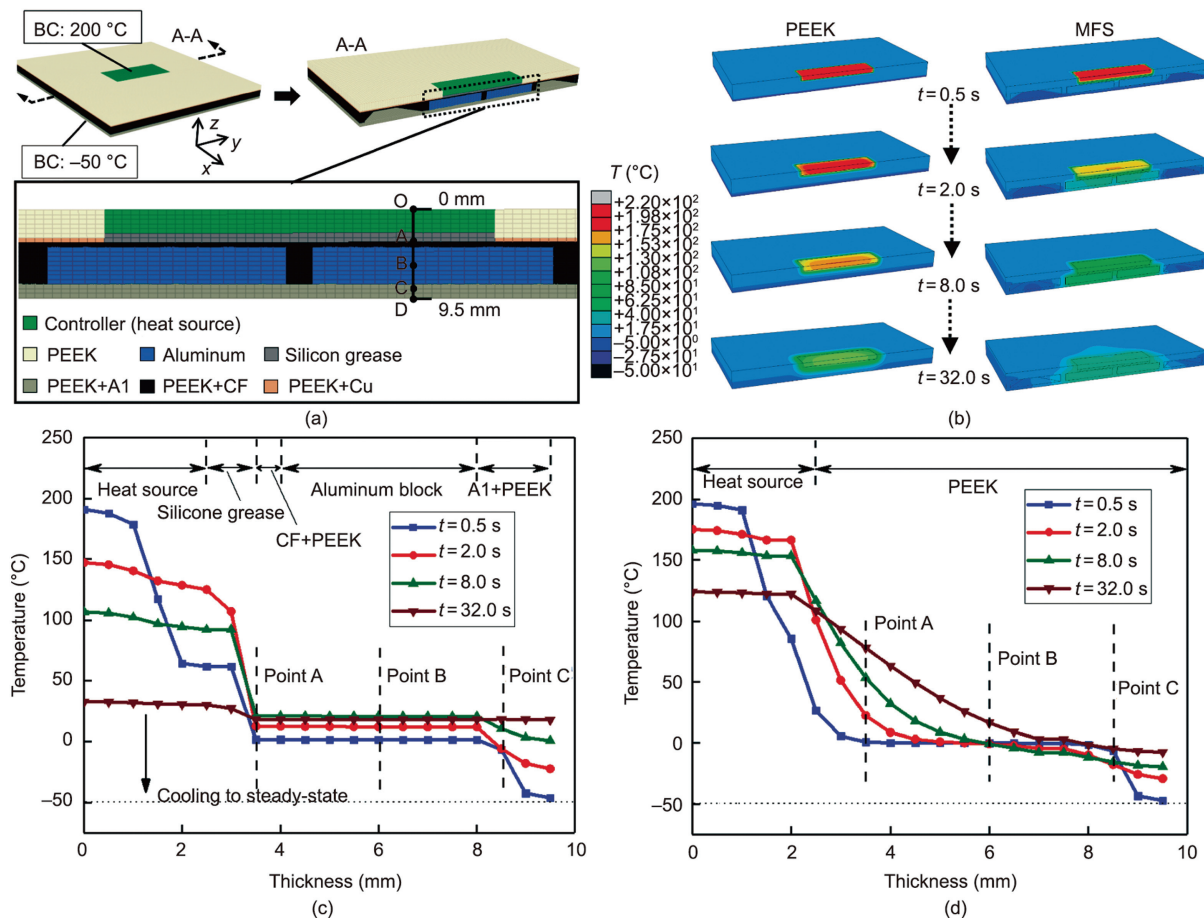


Fig. 5. Thermal analysis of MFS. (a) Finite-element model of MFS; (b) temperature field distributions of half panels at representative times; (c) temperature values of MFS along the thicknesses O–D; (d) temperature values of PEEK corresponding to the same position for comparison. BC: boundary condition.

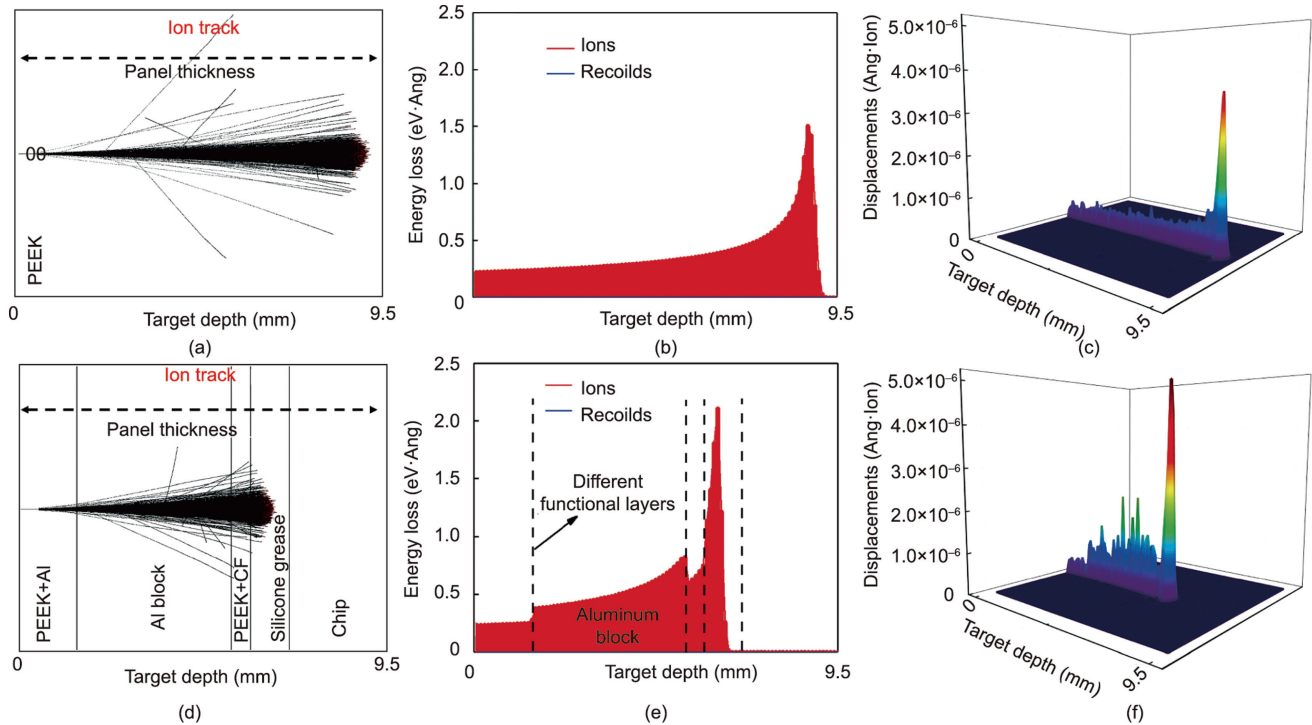


Fig. 6. Radiation-shielding analysis. (a) Tracks of proton implantation along the MFS thickness; (b) ionization damage with energy loss during proton implantation in MFS; (c) displacement damage during proton implantation in MFS; (d–f) corresponding analysis of the PEEK panel. $1 \text{ \AA} = 10^{-10} \text{ m}$.

delocalization of the conjugated π bond in the benzene ring, the MFS design further reduces the ion implantation depth by approximately 27.9%.

The ion implantation depth is affected by the target material. If the excitation process of electrons and atoms is assumed to be irrelevant, the implantation depth D can be expressed as follows [52]:

$$D = \int_0^D \frac{dE}{dE/dx} = \frac{1}{\rho} \int_0^D \frac{dE}{S_n(E) + S_e(E)} \quad (4)$$

where E is the energy loss during ion implantation; x is the integration variable of implantation depth; ρ is the target material density; and $S_n(E)$ and $S_e(E)$ are the blocking cross-sections of the target nucleus and electron, respectively.

Because of the blocking of the target nucleus and electron, the ion collides with the nucleus and electron, causing ionization and displacement damage. Ionization damage will impair the embedded electronic devices; the energy loss caused by ionization is shown in Figs. 6(b) and (e). The embedding of the aluminum block leads to great ion energy loss in the ionization damage. Figs. 6(c) and (f) show the displacement damage distribution in the target material. The displacement damage causes the target atom to leave its original position and move to other polymer chains and lattices, causing degradation of the material properties. This damage is equal to the sum of vacancies and replacement collisions. The vacancies resulting from direct ion collision are the main form of displacement damage in both the PEEK and MFS panels.

5.2. Application in satellite operation

The processes of environment detection, communication, and data transmission are the main working flow of satellites, as shown in Fig. 7(a), and require different modules to perform tasks in cooperation. In this work, due to the difficulty of in-orbit manufacturing and testing, we simplify the satellite assembly and function

verification. Representative modules, such as sensor detection, wireless data transmission, and energy self-supply, are all included.

Diverse MFS modules were designed, as shown in Fig. 7(b). The data detected by sensor DHT11 in the sensor system were transmitted to the Arduino Nano microcontroller unit (MCU) in the control system. The communication microchip in the transmission system uploads the data to the accessed network based on the IEEE 802.11 protocol. Two power modules in the power systems supply energy to the entire system, and one redundant panel is integrated with interfaces for connecting the main load.

The MFS panels can be rapidly manufactured according to the design (Fig. S7 in Appendix A). Separate MFS panels were assembled into a cubic satellite prototype by applying plug-and-play (PnP) mechanisms using a robotic arm, as shown in Fig. 7(c). The panels were connected via the exposed interface and enable the remote monitoring of environmental changes such as temperature and humidity. Status data were detected and uploaded to the cloud by the satellite prototype. Humidification, heating, and drying were applied to induce status changes in the environment. A computer was employed to monitor the status by accessing the cloud network, and data changes in the environment were successfully received in real time, as shown in Fig. 7(d).

The embedded sensors and controllers can be replaced with aerospace-grade products in future applications, which would not add superfluous difficulties to the design and manufacturing. The technology route of on-demand MFS design and manufacturing with advanced materials could serve maintainable space missions. During long-term missions, rapid satellite assembly is expected. Damaged parts in satellites and spacecraft swarms can also be replaced with printed MFS panels. Thus, the proposed design concept and printing technology will lead to an improvement in service life and a reduction in maintenance costs under extreme and complex environments by simplifying the painstaking construction process.

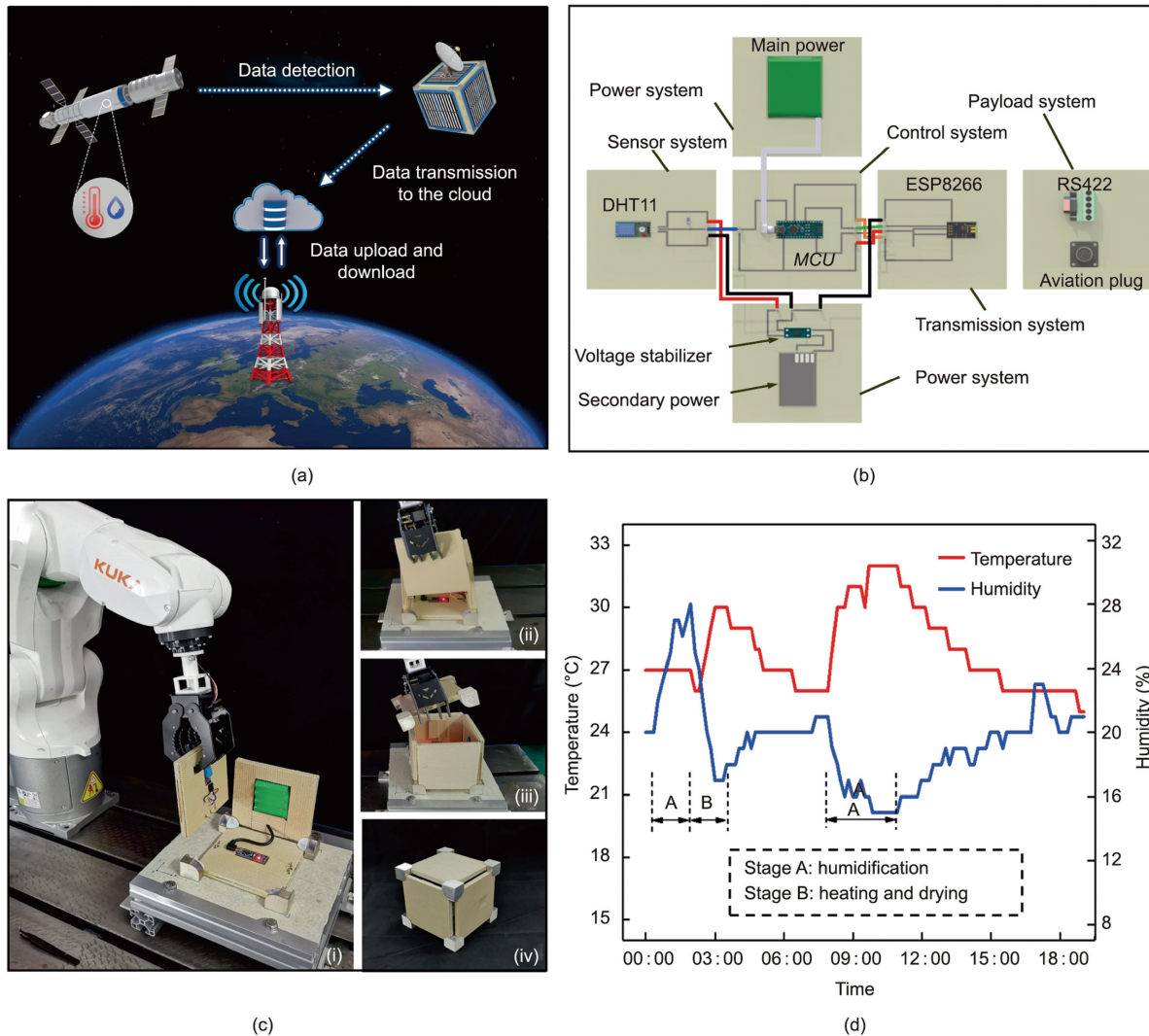


Fig. 7. Satellite prototype design, assembly, and functional verification. (a) Schematic of the function description of a satellite; (b) unfolded design of a satellite prototype and the connections of diverse MFS panels; (c) assembly of satellite prototypes using a robotic arm based on plug-and-play (PnP) mechanisms; (d) detected and received status data of the environment.

6. Conclusions

In this work, we developed a systematic method to design and manufacture customized MFSs, thereby promoting their application in cutting-edge fields. Motivated by the concept of design for manufacturing, we adopted layer regulation to design typical MFSs and then established an optimization model to determine the structural parameters. A high-temperature *in situ* AM technology was developed to print various metal wires or CF-reinforced high-melting-point PEEK composites. In addition, path-planning strategies including a deep Q network (DQN) model and conventional filling rules were implemented for different design areas in the MFS.

The designed and manufactured MFSs not only have diverse functional integration but also contain various performance enhancements of relevant properties. Under bending loads, the stiffness of the MFS is 21.5% higher than that of a pure PEEK substrate but with a lower mass. The first natural frequency of the MFS is greater than 200 Hz, which satisfies the frequency constraints of known launch vehicles. The embedded electrics in the MFS remain functional even after structural elastic deformation during the loading process. The equivalent thermal conductivity

of the MFSs beneath the central heat source is increased by 568%, and the shielding ability against proton radiation is improved by 27.9%, compared with those of PEEK substrates.

The technical route for design and manufacturing proposed herein demonstrates a feasible way to rapidly constitute a variety of MFSs to satisfy specific requirements. As an illustration, MFSs embedded with diverse modules were assembled into a satellite prototype that successfully transmitted the detected data to the cloud through MFSs' collaboration. The outcomes of this work exemplify the possibility of effectively achieving customizable MFSs with remarkable qualities, providing a huge potential impetus for high-performance design and advanced manufacturing.

Authors' contribution

Yan Zhang: conceptualization, investigation, methodology, software, validation, and writing—original draft. Guanyu Zhang: software, project administration, resources, and supervision. Jing Qiao: methodology, validation, resources, and formal analysis. Longqiu Li: conceptualization, investigation, project administration, funding acquisition, and writing—review and editing.

Acknowledgments

This work has been supported by the National Natural Science Foundation of China (51822503, U20A20297, and 51975142), and Key-Area Research and Development Program of Guangdong Province, China (2020B090923003).

Compliance with ethics guidelines

Yan Zhang, Guangyu Zhang, Jing Qiao, and Longqiu Li declare that they have no conflict of interest or financial conflicts to disclose.

Appendix A. Supplementary material

Supplementary data to this article can be found online at <https://doi.org/10.1016/j.eng.2022.11.009>.

References

- Zhang Q, Barri K, Kari SR, Wang ZL, Alavi AH. Multifunctional triboelectric nanogenerator-enabled structural elements for next generation civil infrastructure monitoring systems. *Adv Funct Mater* 2021;31(47):2105825.
- Hensleigh R, Cui H, Xu Z, Massman J, Yao D, Berrigan J, et al. Charge-programmed three-dimensional printing for multi-material electronic devices. *Nat Electron* 2020;3(4):216–24.
- Haque ABMT, Tutika R, Byrum RL, Bartlett MD. Programmable liquid metal microstructures for multifunctional soft thermal composites. *Adv Funct Mater* 2020;30(25):2000832.
- Liu S, Wang W, Xu W, Liu L, Zhang W, Song K, et al. Continuous three-dimensional printing of architected piezoelectric sensors in minutes. *Research* 2022;2022:9790307.
- Sairajan KK, Aglietti GS, Mani KM. A review of multifunctional structure technology for aerospace applications. *Acta Astronaut* 2016;120:30–42.
- Luo L, Zhang F, Leng J. Shape memory epoxy resin and its composites: from materials to applications. *Research* 2022;2022:9767830.
- Chen Q, Lv P, Huang J, Huang TY, Duan H. Intelligent shape-morphing micromachines. *Research* 2021;2021:9806463.
- Aglietti GS, Schwingshackl CW, Roberts SC. Multifunctional structure technology for satellite applications. *Shock Vib Digest* 2007;39(5):381–91.
- Ikeya K, Sakamoto H, Nakanishi H, Furuya H, Tomura T, Ide R, et al. Significance of 3U CubeSat OrigamiSat-1 for space demonstration of multifunctional deployable membrane. *Acta Astronaut* 2020;173:363–77.
- Zuo F, Deng L, Li L, Wang C, Mo Y. Thermal control and shield design for the instrumental module of the X-ray pulsar navigation sensor. In: Kleiman J, editor. *Protection of materials and structures from the space environment*. Cham: Springer International Publishing; 2017. p. 531–41.
- Stevenson TH, Lightsey EG. Design and optimization of a multifunctional 3D-printed structure for an inspector Cubesat. *Acta Astronaut* 2020;170:331–41.
- Levchenko I, Bazaka K, Ding Y, Raitses Y, Mazouffre S, Henning T, et al. Space micropropulsion systems for Cubesats and small satellites: from proximate targets to furthestmost frontiers. *Appl Phys Rev* 2018;5(1):011104.
- Gu D, Shi X, Poprawe R, Bourell DL, Setchi R, Zhu J. Material-structure-performance integrated laser-metal additive manufacturing. *Science* 2021;372:6545.
- Hasan M, Zhao J, Jiang Z. Micromanufacturing of composite materials: a review. *Int J Extreme Manuf* 2019;1(1):012004.
- Yang Y, Wang Z, He Q, Li X, Lu G, Jiang L, et al. 3D printing of nacre-inspired structures with exceptional mechanical and flame-retardant properties. *Research* 2022;2022:9840574.
- Galos J, Best AS, Mouritz AP. Multifunctional sandwich composites containing embedded lithium-ion polymer batteries under bending loads. *Mater Des* 2020;185:108228.
- Ren B, Yuen G, Deng S, Jiang L, Zhou D, Gu L, et al. Multifunctional optoelectronic device based on an asymmetric active layer structure. *Adv Funct Mater* 2019;29(17):1807894.
- Battaia O, Dolgui A, Heragu SS, Meerkov SM, Tiwari MK. Design for manufacturing and assembly/disassembly: joint design of products and production systems. *Int J Prod Res* 2018;56(24):7181–9.
- Fortunet C, Durieux S, Chanal H, Duc E. DFM method for aircraft structural parts using the AHP method. *Int J Adv Manuf Technol* 2018;95(1–4):397–408.
- Guo D, Lu Y. Overview of extreme manufacturing. *Int J Extreme Manuf* 2019;1(2):020201.
- Ren W, Xu J, Lian Z, Sun X, Xu Z, Yu H. Localized electrodeposition micro additive manufacturing of pure copper microstructures. *Int J Extreme Manuf* 2022;4(1):015101.
- Kaur M, Kim TH, Kim WS. New frontiers in 3D structural sensing robots. *Adv Mater* 2021;33(19):e2002534.
- Chen B, Chen L, Du B, Liu H, Li W, Fang D. Novel multifunctional negative stiffness mechanical metamaterial structure: tailored functions of multi-stable and compressive mono-stable. *Compos Part B Eng* 2021;204:108501.
- Liu S, Li Q, Liu J, Chen W, Zhang Y. A realization method for transforming a topology optimization design into additive manufacturing structures. *Engineering* 2018;4(2):277–85.
- Liu G, He Y, Liu P, Chen Z, Chen X, Wan L, et al. Development of bioimplants with 2D, 3D, and 4D additive manufacturing. *Mater Des* 2020;6(11):1232–43.
- Feng H, Liu Y, Feng L, Zhan L, Meng S, Ji H, et al. Additively manufactured flexible electronics with ultrabroad range and high sensitivity for multiple physiological signals' detection. *Research* 2022;2022:9871489.
- Zeng C, Liu L, Bian W, Leng J, Liu Y. Bending performance and failure behavior of 3D printed continuous fiber reinforced composite corrugated sandwich structures with shape memory capability. *Compos Struct* 2021;262:113626.
- Espalin D, Muse DW, MacDonald E, Wicker RB. 3D printing multifunctionality: structures with electronics. *Int J Adv Manuf Technol* 2014;72(5–8):963–78.
- MacDonald E, Espalin D, Doyle D, Muñoz J, Ambriz S, Coronel J, et al. Fabricating patch antennas within complex dielectric structures through multi-process 3D printing. *J Manuf Process* 2018;34:197–203.
- MacDonald E, Wicker R. Multiprocess 3D printing for increasing component functionality. *Science* 2016;353:6307.
- Zhu Z, Ng DWH, Park HS, McAlpine MC. 3D-printed multifunctional materials enabled by artificial-intelligence-assisted fabrication technologies. *Nat Rev Mater* 2021;6(1):27–47.
- Loke G, Yuan R, Rein M, Khudiyev T, Jain Y, Joannopoulos J, et al. Structured multimaterial filaments for 3D printing of optoelectronics. *Nat Commun* 2019;10(1):4010.
- Echsel M, Springer P, Hümbert S. Production and planned in-orbit qualification of a function-integrated, additive manufactured satellite sandwich structure with embedded automotive electronics. *CEAS Space J* 2021;13:111–8.
- Sacco E, Moon SK. Additive manufacturing for space: status and promises. *Int J Adv Manuf Technol* 2019;105(10):4123–46.
- Hamad A, Mian A, Khondaker SI. Direct-write inkjet printing of nanosilver ink (UTDag) on PEEK substrate. *J Manuf Process* 2020;55:326–34.
- Thiruchitrambalam M, Bubesh Kumar D, Shanmugam D, Jawaid M. A review on PEEK composites—manufacturing methods, properties and applications. *Mater Today Proc* 2020;33:1085–92.
- Madito MJ, Hlatshwayo TT, Skuratov VA, Mtshali CB, Manyala N, Khumalo ZM. Characterization of 167 MeV Xe ion irradiated n-type 4H-SiC. *Appl Surf Sci* 2019;493:1291–8.
- Wang C, Zhang L, Fang Y, Sun W. Design, characterization, and 3D printing of cardiovascular stents with zero Poisson's ratio in longitudinal deformation. *Engineering* 2021;7(7):979–90.
- Hou Z, Tian X, Zhang J, Zheng Z, Zhe L, Li D, et al. Optimization design and 3D printing of curvilinear fiber reinforced variable stiffness composites. *Compos Sci Technol* 2021;201:108502.
- Matsuzaki R, Ueda M, Namiki M, Jeong TK, Asahara H, Horiguchi K, et al. Three-dimensional printing of continuous-fiber composites by in-nozzle impregnation. *Sci Rep* 2016;6(1):23058.
- Mosleh N, Rezadoust AM, Dariushi S. Determining process-window for manufacturing of continuous carbon fiber-reinforced composite using 3D-printing. *Mater Manuf Process* 2020;36(4):1–10.
- Wang T, Li N, Link G, Jelonnek J, Fleischer J, Dittus J, et al. Load-dependent path planning method for 3D printing of continuous fiber reinforced plastics. *Compos Part A Appl Sci Manuf* 2021;140:106181.
- Peterson AM. Review of acrylonitrile butadiene styrene in fused filament fabrication: a plastics engineering-focused perspective. *Addit Manuf* 2019;27:363–71.
- Cano-Vicent A, Tambuwala MM, Hassan SS, Barh D, Aljabali AAA, Birkett M, et al. Fused deposition modelling: current status, methodology, applications and future prospects. *Addit Manuf* 2021;47:102378.
- Feng C, Hemantha Rajapaksha CP, Jáklí A. Ionic elastomers for electric actuators and sensors. *Engineering* 2021;7(5):581–602.
- Kim C, Sullivan C, Hillstrom A, Wicker R. Intermittent embedding of wire into 3D prints for wireless power transfer. *Int J Precis Eng Manuf* 2021;22(5):919–31.
- Kim C, Espalin D, Liang M, Xin H, Cuaron A, Varela I, et al. 3D printed electronics with high performance, multi-layered electrical interconnect. *IEEE Access* 2017;5:25286–94.
- Rinaldi M, Cecchini F, Pigliaru L, Ghidini T, Lumaca F, Nanni F. Additive manufacturing of polyether ether ketone (PEEK) for space applications: a nanosat polymeric structure. *Polymers* 2020;13(1):11.
- Fajardo I, Lidtke A, Bendoukha S, Gonzalez-Llorente J, Rodríguez R, Morales R, et al. Design, implementation, and operation of a small satellite mission to explore the space weather effects in LEO. *Aerospace* 2019;6(10):108.
- Gülhan A, Braun S. An experimental study on the efficiency of transpiration cooling in laminar and turbulent hypersonic flows. *Exp Fluids* 2011;50(3):509–25.
- Demyanov V. In: Becedas J, editor. *Satellites missions and technologies for geosciences*. London: IntechOpen; 2020.
- Li H, Yang J, Tian F, Li X, Dong S. Study on the microstructure of polyether ether ketone films irradiated with 170 keV protons by grazing incidence small angle X-ray scattering (GISAXS) technology. *Polymers* 2020;12(11):2717.